

Collective Directional Locking of Colloidal Monolayers on a Periodic Substrate

Ralph L. Stoop,¹ Arthur V. Straube,^{2,3,1} Tom H. Johansen,^{4,5} and Pietro Tierno^{1,6,7,*}

¹*Departament de Física de la Matèria Condensada, Universitat de Barcelona, Barcelona, Spain*

²*Department of Mathematics and Computer Science, Freie Universität Berlin, Berlin, Germany*

³*Group “Dynamics of Complex Materials”, Zuse Institute Berlin, Berlin, Germany*

⁴*Department of Physics, University of Oslo, P. O. Box 1048 Blindern, 0316 Oslo, Norway*

⁵*Institute for Superconducting and Electronic Materials,*

University of Wollongong, Northfields Avenue, Wollongong, NSW 2522, Australia

⁶*Universitat de Barcelona Institute of Complex Systems (UBICS), Universitat de Barcelona, Barcelona, Spain*

⁷*Institut de Nanociència i Nanotecnologia, IN²UB, Universitat de Barcelona, Barcelona, Spain.*

(Dated: February 18, 2022)

We investigate the directional locking effects that arise when a monolayer of paramagnetic colloidal particles is driven across a triangular lattice of magnetic bubbles. We use an external rotating magnetic field to generate a two dimensional traveling wave ratchet forcing the transport of particles along a direction that intersects two crystallographic axes of the lattice. We find that, while single particles show no preferred direction, collective effects induce transversal current and directional locking at high density via a spontaneous symmetry breaking. The colloidal current may be polarized via an additional bias field that makes one transport direction energetically preferred.

PACS numbers: 05.60.Cd, 82.70.Dd, 75.70.Kw

Introduction. Understanding the dynamic states that emerge from interacting particles driven across periodic potentials is relevant for a great variety of condensed matter systems [1–4], ranging from electron scattering [5] to vortices in superconductors [6, 7], artificial spin ice [8], skyrmions [9], granular [10] and active matter [11]. Beside the fundamental insights, controlling the flow of microscale systems across ordered landscapes can have direct technological applications such as particle sorting and fractionation [12–18], processes that are relevant to both microfluidics [19] and biotechnology [20].

An astonishing effect that arises when the particles are driven through a regular array of obstacles or potential wells is directional locking [21, 22]. Such phenomenon occurs when these particles move along periodic trajectories that are commensurate with the underlying lattice, in general not aligned with the direction of the driving force. An experimentally accessible model system that allows investigating directional locking in real time and space, is based on the use of microscopic colloidal particles. This result from our ability to develop periodic potentials at the micro-scale using a variety of external means. In previous experimental realizations directional locking has received much attention at the level of single particles, and it manifested with the presence of a Devil’s staircase structure in the particle migration angle [21, 23]. More recently, orientational and directional locking were observed for stiff clusters of microscopic particles driven by gravity across a periodic array of holes, and the resulting complex dynamics followed from competing symmetries between the two crystalline surfaces [24].

For disperse and interacting multi-body systems, directional locking effect may emerge even in the most symmetric situation, i.e. when the particles are driven exactly at the middle of two crystallographic axes of the

lattice. A related example in condensed matter is given by an ensemble of vortices in high T_c superconductors forced to move across a honeycomb lattice of pinning sites. Numerical simulations of the vortex system predict the emergence of a transversal current which result from the formation of dimeric state in the interstitial region of the lattice [25]. We also note that directional locking effects have been recently reported on quasiperiodic substrates in experiments [26] and on quasicrystalline substrates in simulations [27], although these studies have been limited to fixed density of the interacting particles.

Here we experimentally observe collective, density-dependent locking effects and transversal currents when a monolayer of paramagnetic colloidal particles is driven across a lattice of cylindrical ferromagnetic domains. We show that, when the particles are driven along a direction that intersects two crystallographic axes, collective interactions polarize the particle current along a preferred direction, not aligned along the driving one. Such direction results from a spontaneous symmetry breaking, and the corresponding velocity density curve displays a bifurcation diagram with two branches that can be destabilized via an additional bias field. Although directional locking induced by collective interactions has been predicted in different theoretical works [12, 25, 28–30], we provide the first experimental observation of this general effect.

Experiment. As magnetic substrate we use a ferrite garnet film (FGF) with uniaxial anisotropy which was synthesized by liquid phase epitaxial growth [31] on a (111) oriented gadolinium gallium garnet (GGG) substrate. The FGF has composition $Y_{2.5}Bi_{0.5}Fe_{5-q}Ga_qO_{12}$ ($q = 0.51$), saturation magnetization $M_s = 1.3 \cdot 10^4 \text{ Am}^{-1}$ and it displays a triangular lattice of cylindrical domains or “magnetic bubbles”, with diameter $D = 2.4 \mu\text{m}$ at zero field, and lattice constant $a = 3.4 \mu\text{m}$, see Fig.1(a). These

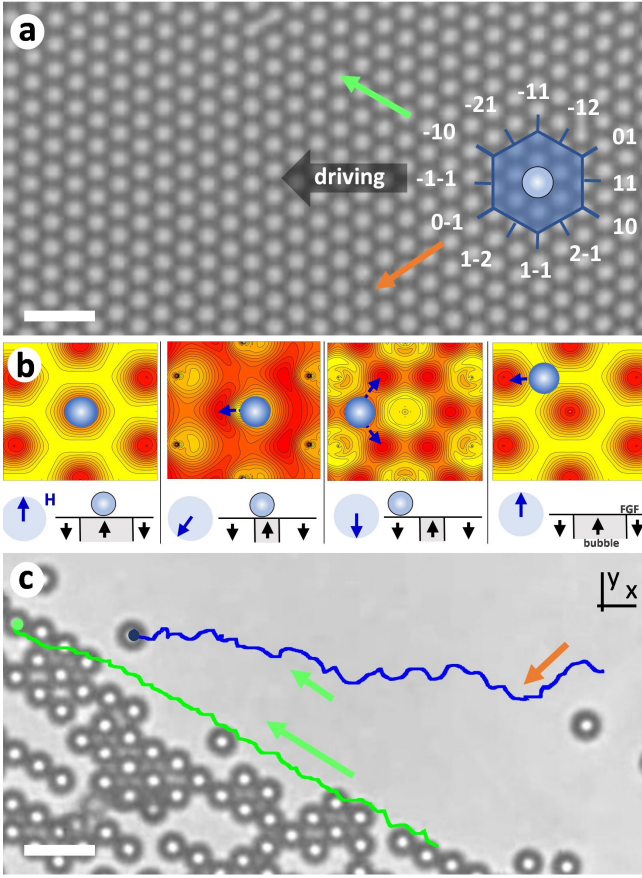


FIG. 1. (a) Polarization microscope image showing a small portion of a magnetic bubble lattice with a schematic of the 12 possible directions. The particles are driven toward left along the $-1-1$ direction. \hat{a}_{\pm} ; the basic lattice vectors are chosen as $\hat{a}_{\pm} = (\sqrt{3}a/2, \pm a/2)$. Scale bar is $10\mu\text{m}$. (b) Energy landscape of the magnetic lattice calculated at an elevation $z = 0.7a$ ($H_0 = 0.06M_s$) for $t = 0$, $t = 3\pi/(4\omega)$, $t = \pi/\omega$ and $t = 2\pi/\omega$ (from left to right, the particle moves from right to left). Schematics at the bottom shows one bubble in the FGF during the different phases of the applied field. See [32] for details on the calculation. (c) Microscope image of the same region showing paramagnetic colloids driven towards left by a rotating field with $H_0 = 600\text{Am}^{-1}$, $\omega = 25.1\text{rads}^{-1}$ and $\beta = -1/3$. Superimposed are two trajectories of an individual particle (blue path) and one in a dense collection (green path). Scale bar is $10\mu\text{m}$, see also Video1 in [32].

cylindrical domains where generated using a strong gradient field $\nabla B \sim 0.2\text{T/m}$ perpendicular to the film before the experiments, and can be visualized by the polar Faraday effect, see Video1 in [32]. For low amplitudes, the size of the bubbles can be linearly tuned by a perpendicular field $\mathbf{H}^{\text{ext}} = H_z \hat{z}$, according to the relation $D = 2a\sqrt{(H_z/M_s + 1) \frac{\sin(\pi/3)}{2\pi}}$. On this film we deposit a water dispersion of paramagnetic colloidal particles with diameter $d = 2.8\mu\text{m}$ (Dynabeads M-270) and magnetic volume susceptibility $\chi = 0.4$. In contrast to a previous

work [33], we create here a periodic substrate composed of magnetic bubbles small enough to accommodate only one particle per unit cell. Before the experiments, the FGF is coated with a $1\mu\text{m}$ thick layer of a positive photoresist (AZ-1512, Microchem MA) using spin coating and UV photo-crosslinking [34]. We use digital video microscopy [35] to keep track of the particle positions $(x_i(t), y_i(t))$ with $i = 1 \dots N$, and measure the instantaneous velocities $v_{x,y}$, here $v_x(t) = \frac{1}{N} \sum_i \frac{dx_i}{dt}$, and their mean values taken in the stationary regime [36].

Particle transport. Over the FGF plate we displace the colloidal particles via an external rotating magnetic field elliptically polarized in the (\hat{x}, \hat{z}) plane, $\mathbf{H}^{\text{ext}} = [-H_x \sin(\omega t) \hat{e}_x + H_z \cos(\omega t) \hat{e}_z]$, with frequency ω and amplitudes (H_x, H_z) . The total amplitude is given by $H_0 = \sqrt{(H_x^2 + H_z^2)}/2$ and the ellipticity parameter by $\beta = (H_x^2 - H_z^2)/(H_x^2 + H_z^2)$ with $\beta \in [-1, 1]$. The applied field modulates the stray field \mathbf{H}^{sub} on the FGF substrate, see [32] for details, and generates a two dimensional traveling wave ratchet which drag along the particles in a deterministic way (thermal noise is negligible). For $\omega < 31.4\text{rads}^{-1}$, the transport is field synchronized, and the particles move ballistically with the speed of the traveling wave, $v_m = a\omega/(2\pi)$, more details are given in [32]. Throughout this work, we vary mainly the normalized particle density $\rho = (Nd)/A$ within the observation area A , and keep $\omega = 25.1\text{rads}^{-1}$ constant, which corresponds to a synchronous speed $\langle v_x \rangle = \sqrt{3}v_m/2 \simeq -11\mu\text{ms}^{-1}$. The field parameters are fixed to $H_0 = 600\text{Am}^{-1}$ and $\beta = -1/3$.

The single particle transport can be understood by calculating how the energy landscape of a paramagnetic colloid is altered by the applied field during one field cycle, Fig.1(b). When the field is parallel to the bubble magnetization, $\mathbf{H}^{\text{ext}} = H_z \hat{z}$ ($t = 0$), the energy minimum, and thus the particle, is located at the center of the magnetic bubble. For $t = \pi/(2\omega)$ and $\mathbf{H}^{\text{ext}} = -H_x \hat{x}$, the in-plane field H_x deforms the landscape translating the particle to the interstitial region. When the field is anti-parallel to the bubble magnetization ($t = \pi/\omega$, $\mathbf{H}^{\text{ext}} = -H_z \hat{z}$), it induces the nucleation of six equal energy minima at the interstitial region. For $t > \pi/\omega$, the interstitial minimum along the $-1-1$ direction start to disappear faster than the other two along the -10 , and $0-1$ crystallographic directions, as shown in FigS2. These two minima produce two equivalent pathways along which the particle can be transported to reach one of the two closest magnetic bubbles ($t = \pi/\omega$). Since these pathways are energetically equivalent, the choice of the particle is given by its initial position in the bubble minima, which is influenced by noise as thermal fluctuations. As a result, the single particle transport displays no preference on the transversal (\hat{y}) direction.

Results. To investigate directional locking effects we orient the magnetic substrate such that the driving direction ($\hat{x} < 0$) is exactly between the two symmetry axes,

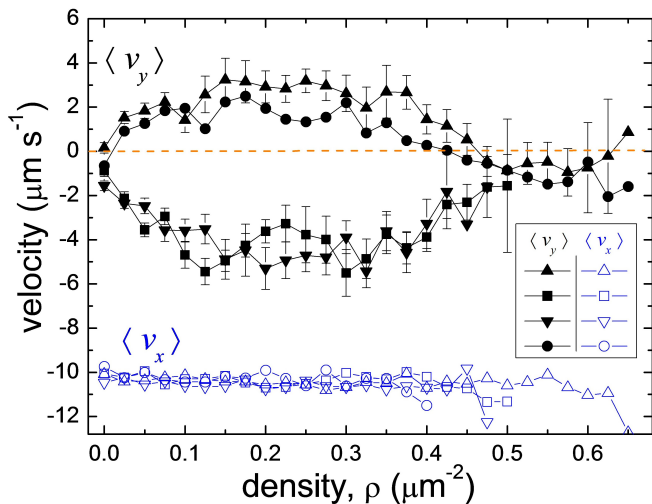


FIG. 2. Longitudinal velocity $\langle v_x \rangle$ (blue open symbols) and transversal one $\langle v_y \rangle$ (black filled symbols) versus normalized particle density ρ for paramagnetic colloids driven toward left. Error bars are obtained from the statistical analysis of different experimental realizations.

-10 and $0 - 1$, Fig.1(a) [37]. In this situation, single particles display erratic trajectories, composed by an alternation of up and down interstitial jumps and a vanishing transversal velocity $\langle v_y \rangle = 0$, Fig.1(c). However, we find that for denser systems the colloidal current polarizes following one of the two crystallographic directions. For example, in Fig. 1(c) the dense collection of particles flows along the -10 direction ($\langle v_y \rangle > 0$). The observed phenomenon is rather robust, and lasts as long as the particle density ρ or the applied field are kept constant. The chosen direction results from dynamically symmetry breaking: switching off and later on the rotating field \mathbf{H} can induce transport along the complementary crystallographic direction, $0 - 1$, with a negative velocity $\langle v_y \rangle < 0$. Moreover we find that along the chosen path, the colloidal flow is highly ordered, with few particle rearrangements. Now the particles form elongated and compact clusters which keep their shape during motion, as shown in Fig.S3 in [32], where we report the corresponding evolution of mean cluster size and the degree of clustering.

Fig.2 shows the current density diagram measured in four different experiments, all of which conducted by transporting the paramagnetic colloids towards left, $\langle v_x \rangle < 0$, corresponding images are illustrated in the four left panel of Fig.3. We measure a bifurcation diagram showing two nearly symmetric branches starting from $\rho \sim 0.05$, and that reach a maximum separation speed of $\sim 8 \mu\text{m s}^{-1}$ for $\rho \in [0.17, 0.27]$. In all cases, the mean longitudinal velocity remains constant to $\langle v_x \rangle = -10.3 \mu\text{m s}^{-1}$. Above $\rho \sim 0.5$ the two branches merge and the bistability is lost for large clusters. In this situation, the colloidal particles form a percolating net-

work that covers the whole potential landscape. Even if the particle density is below close packing, the colloids have now nearest neighbors which impede the formation of polarized clusters moving along a defined crystallographic axis. Further, we note that in the experimental data the two branches are not exactly centered at $\langle v_y \rangle = 0$ indicating that the magnetic field distribution is not exactly symmetric, due to the presence of imperfections in the bubble lattice, as double magnetic domains. These imperfections create dislocation in the bubble array which may induce change in the crystallographic direction of the driven clusters, see also Fig.S3 in [32] for

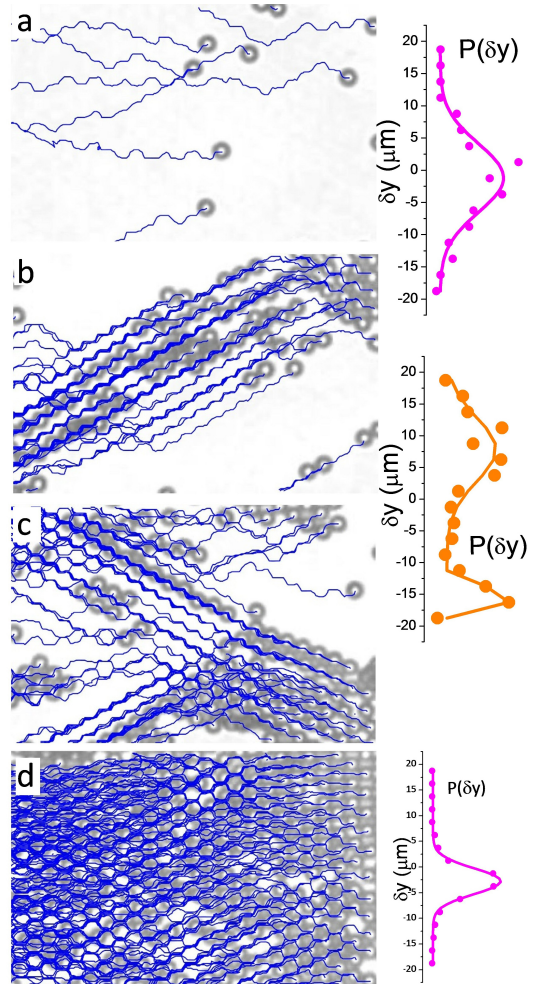


FIG. 3. Experimental images with superimposed particle trajectories for: (a) $\rho = 0.02$; (b) $\rho = 0.23$ (c) $\rho = 0.16$; (d) $\rho = 0.58$. Lateral graphs show the distribution of the transversal displacement of the particles $P(\delta y)$ for three different regions of the diagram with $\rho < 0.025$ (top left), $\rho \in [0.55, 0.65]$ (bottom left) and $\rho \in [0.17, 0.27]$ (right). The $P(\delta y)$ at the top ($R^2 = 0.85$) and at the bottom ($R^2 = 0.99$) are fitted with a Gaussian distribution, while the middle curve is a bimodal fit ($R^2 = 0.82$), being R^2 the coefficient of determination.

the case of Figs.3(b,c). We further measure the distribution of lateral displacement $P(\delta y)$ for all set of data, as shown in Fig.3. Here we find that $P(\delta y)$ are Gaussian for both low ($\rho < 0.025$, Fig.3(a)) and high ($\rho \in [0.55, 0.65]$, Fig.3(d)) densities where the branches merge. However at high density the width of the Gaussian ($\sigma = 5\mu m$) reduces by half the value at low density ($\sigma = 10.6\mu m$) due to the high concentration of particles, and the corresponding reduction of their lateral mobility. In contrast, for intermediate density ($\rho \in [0.17, 0.27]$, Figs.3(b,c)) we find a bimodal distribution, which reflects the bistability reported in Fig.2.

The transverse polarization produces a dynamical synchronization process between nearest propelling particles in the clusters. We quantify this effect in Fig.4 by measuring the average distance between nearest neighbor (nn) particles, $\langle \Delta r \rangle = \langle r_{ij}(t) - r_{ij}(0) \rangle_{nn}$, being $r_{ij} = |\mathbf{r}_i - \mathbf{r}_j|$ and \mathbf{r}_i the position of particle i . For dilute density, the particles are far away and dipolar interactions are unable to form the clusters, thus $\langle \Delta r \rangle$ is observed to increase over with time in our experimental area. For intermediate densities ($\rho = 0.18$) the particles form elongated clusters, and the lateral jumps of the composing particles across the interstitial region (Fig. 1(b)) are coherently synchronized. In this situation the average distance between two particles is of the order of the lattice constant a , where $r_{ij} \sim a \forall t$, $\langle \Delta r \rangle \rightarrow 0$. At high density the directional locking is lost and the particles within the percolating structure display uncorrelated upward and downward lateral jumps. Thus, $\langle \Delta r \rangle$ raises but slowly due to the high particle density.

The collective directional locking at intermediate ρ results from the formation of compact clusters kept by at-

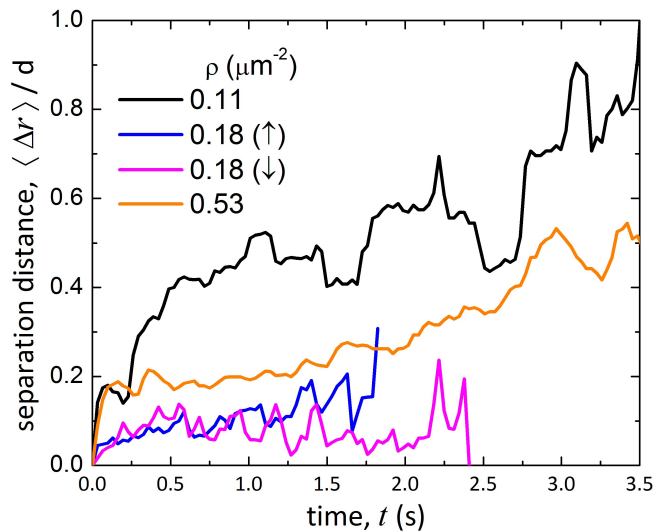


FIG. 4. Normalized average distance between nearest neighbours $\langle \Delta r \rangle$ versus time calculated for four densities.

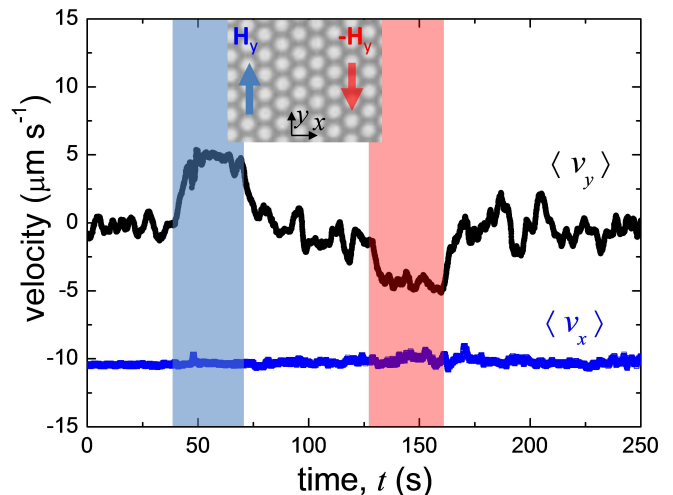


FIG. 5. Velocities versus time for a dilute system driven to the left, where density is slowly decreasing in time from $\rho = 0.06$ ($t = 0$ s) to $\rho = 0.06$ ($t = 250$ s). The shaded regions indicate the presence of an additional magnetic field $H_y = 200 \text{Am}^{-1}$ (blue) and $-H_y$ (pink). Right graph denotes the corresponding evolution of the normalized particle density ρ . Inset shows the direction of the applied bias fields with respect to the magnetic lattice.

tractive dipolar interactions. Via approximate expressions of the magnetic field, see [32] for details, the dipolar interaction between two particles with coordinates $\mathbf{r}_1 = (x_1, y_1)$ and $\mathbf{r}_2 = (x_2, y_2) = \mathbf{r}_1 - \mathbf{a}_\pm$, i.e. separated by one lattice constant a and aligned along a crystallographic axis, $\mathbf{a}_\pm = (\sqrt{3}a/2, \pm a/2)$ is reduced to

$$U_d(\mathbf{r}_1) \propto F_{xx}(1 - 3\hat{x}_{12}^2) + F_{zz} - 3F_{xy}\hat{x}_{12}\hat{y}_{12}, \quad (1)$$

where $F_{xy} = 2H_x^{\text{ext}}(t)H_y^{\text{sub}}(\mathbf{r}_1)$ and similarly for F_{xx} , F_{zz} , and $\hat{x}_{12} = \sqrt{3}/2$, $\hat{y}_{12} = \pm 1/2$. Potential (1) has a hexagonal structure with attraction along the crystallographic axes. These interactions are caused by the interplay between stray field and external modulation while evolving in time, and is a complex and richer effect than that reported before [38]. Our model neglects hydrodynamic interactions suggesting that magnetic forces dominate the dynamics of the system.

For intermediate densities, the dynamical state of our driven monolayer is bistable, and switching between them can be controlled by an additional bias field H_y superimposed to the driving one. We demonstrate this feature in Fig.5, where the particle velocities are plotted as a function of time for a low density case ($\rho \sim 0.1$) where $\langle v_y \rangle = 0$, while $\langle v_x \rangle = -10 \mu\text{ms}^{-1}$. The addition of a static, transversal component $-H_y$ (H_y) to the rotating field during two time intervals $t \in [36.5, 70.6]$ s ($t \in [128.9, 161.9]$ s) polarizes the colloidal current along the 0-1 (-10) direction with $\langle v_y \rangle = -4.9 \mu\text{ms}^{-1}$ ($\langle v_y \rangle = 4.6 \mu\text{ms}^{-1}$) while the longitudinal current remains prac-

tically unaffected. Inspection of how the bias changes the two energy landscapes, reveals that the applied field produces a preferred energetic path during the particle excursion process, creating interstitial wells with unequal depths and thus transversal rectification along the bias direction. The polarization effect enables to selectively control the transversal rectification process, in contrast to the spontaneously chosen transport path in absence of bias. We also stress the fact that our colloidal current is generated via time-modulated homogeneous magnetic fields, and not via external field gradient as in magnetophoresis [39], that would impede the observation and control of transversal current across the lattice.

To conclude, we demonstrate spontaneous directional locking that emerges by collective interactions when a monolayer of colloidal particles is driven across a periodic substrate. Our results have been obtained with a specially prepared single crystal uniaxial ferromagnetic thin film, however they are more general and can be observed in other condensed matter systems characterized by interacting particles driven across corrugated landscape. Example of transverse response and bistability effects have been reported in the past for vortex matter in high T_c superconductors [25] or electron scattering [40]. Also, the understanding and control of sliding process between particles on corrugated substrate may be of interest for studying friction and adhesion phenomena [41]. Here we add a mesoscopic model system for locking effects where particle currents and fluctuations can be investigated in real time/space and controlled by an external field.

We thank Thomas M. Fischer for inspiring discussions. R. L. S. acknowledges support from the Swiss National Science Foundation grant No. 172065. A. V. S. was partially supported by the Deutsche Forschungsgemeinschaft (DFG, German Research Foundation) through the grant SFB 1114, project C01 and from MATH+: the Berlin Mathematics Research Center (under Germany's Excellence Strategy, EXC-2046/1 project ID: 390685689), project EF4-4. P. T. acknowledge support from the ERC Grant "ENFORCE" (No. 811234), MINECO (FIS2016-78507-C2-2-P, ERC2018-092827) and Generalitat de Catalunya under program "Icrea Academia".

* ptierno@ub.edu

- [1] P. Hänggi and F. Marchesoni, *Rev. Mod. Phys.*, **81**, 387 (2009).
- [2] A. Vanossi, N. Manini, M. Urbakh, S. Zapperi, and E. Tosatti, *Rev. Mod. Phys.*, **85**, 529 (2013).
- [3] C. Reichhardt and C. J. O. Reichhardt, *Rep. Prog. Phys.*, **80**, 026501 (2017).
- [4] C. Reichhardt and C. J. O. Reichhardt, *Rep. Prog. Phys.*, **80**, 026501 (2017).
- [5] W. Kuehn, P. Gaal, K. Reimann, M. Woerner, T. Elsaesser, and R. Hey, *Phys. Rev. Lett.*, **104**, 146602 (2010).
- [6] M. Baert, V. V. Metlushko, R. Jonckheere, V. V. Moshchalkov, and Y. Bruynseraede, *Phys. Rev. Lett.*, **74**, 3269 (1995).
- [7] K. Harada, O. Kamimura, H. Kasai, T. Matsuda, A. Tonomura, and V. V. Moshchalkov, *Science*, **274**, 1167 (1996).
- [8] Y.-L. Wang, X. Ma, J. Xu, Z.-L. Xiao, A. Snezhko, R. Divan, L. E. Ocola, J. E. Pearson, B. Janko, and W.-K. Kwok, *Nat. Nano.*, **13**, 560565 (2018).
- [9] C. Reichhardt, D. Ray, and C. J. O. Reichhardt, *Phys. Rev. B*, **98**, 134418 (2018).
- [10] N. Kumar, H. Soni, S. Ramaswamy, and A. K. Sood, *Nat. Comm.*, **5**, 4688 (2014).
- [11] C. Bechinger, R. Di Leonardo, H. Löwen, C. Reichhardt, G. Volpe, and G. Volpe, *Rev. Mod. Phys.*, **88**, 045006 (2016).
- [12] C. Reichhardt and C. J. Olson Reichhardt, *Phys. Rev. E*, **69**, 041405 (2004).
- [13] L. R. Huang, E. C. Cox, R. H. Austin, and J. C. Sturm, *Science*, **304**, 987 (2004).
- [14] A. M. Lacasta, J. M. Sancho, A. H. Romero, and K. Lindenberg, *Phys. Rev. Lett.*, **94**, 160601 (2005).
- [15] D. Speer, R. Eichhorn, and P. Reimann, *Phys. Rev. Lett.*, **102**, 124101 (2009).
- [16] D. Speer, R. Eichhorn, and P. Reimann, *Phys. Rev. Lett.*, **105**, 090602 (2010).
- [17] R. Eichhorn, *Phys. Rev. Lett.*, **105**, 034502 (2010).
- [18] D. Reguera, A. Luque, P. S. Burada, G. Schmid, J. M. Rubí, and P. Hänggi, *Phys. Rev. Lett.*, **108**, 020604 (2012).
- [19] M. P. MacDonald, G. C. Spalding, and K. Dholakia, *Nature*, **426**, 421 (2003).
- [20] A. Davis, D. W. Inglis, K. J. Morton, D. A. Lawrence, L. R. Huang, S. Y. Chou, J. C. Sturm, and R. H. Austin, *Proc. Natl. Acad. Sci. USA*, **103**, 14779 (2006).
- [21] P. T. Korda, M. B. Taylor, and D. G. Grier, *Phys. Rev. Lett.*, **89**, 128301 (2002).
- [22] J. Koplik and G. Drazer, *Phys. Fluids*, **22**, 052005 (2010).
- [23] M. Balvin, E. Sohn, T. Iracki, G. Drazer, and J. Frechette, *Phys. Rev. Lett.*, **103**, 078301 (2009).
- [24] X. Cao, E. Panizon, A. Vanossi, N. Manini, and C. Bechinger, *Nat. Physics*, **15**, 776780 (2019).
- [25] C. Reichhardt and C. J. O. Reichhardt, *Phys. Rev. Lett.*, **100**, 167002 (2008).
- [26] T. Bohlein and C. Bechinger, *Phys. Rev. Lett.*, **109**, 058301 (2012).
- [27] C. Reichhardt and C. J. Olson Reichhardt, *Phys. Rev. Lett.*, **106**, 060603 (2011).
- [28] C.-S. Lee, B. Jankó, I. Derényi, and A.-L. Barabási, *Nature*, **400**, 337 (1999).
- [29] C. Reichhardt and C. J. O. Reichhardt, *Europhys. Lett.*, **68**, 303 (2004).
- [30] M. L. Latimer, G. R. Berdiyrov, Z. L. Xiao, W. K. Kwok, and F. M. Peeters, *Phys. Rev. B*, **85**, 012505 (2012).
- [31] P. Tierno, F. Sagués, T. H. Johansen, and T. M. Fischer, *Phys. Chem. Chem. Phys.*, **11**, 9615 (2009).
- [32] See Supplemental Material [url] for more details on the experimental system and four video clips illustrating the particle dynamics. The Supplemental Material includes Refs. [38, 42–44].
- [33] P. Tierno and T. M. Fischer, *Phys. Rev. Lett.*, **112**,

- 048302 (2014).
- [34] This procedure avoids that the colloidal particles stick to the domain walls of the FGF due to their magnetic attraction. The gravitational length of the particles can be estimated as $h_g = k_B T / (Vg\Delta\rho) = 61nm$, thus much smaller than the particle size, and even in absence of attraction the system can be considered as effectively two-dimensional.
- [35] J. C. Crocker and D. G. Grier, *J. Colloid Interface Sci.*, **179**, 298 (1996).
- [36] We use an upright microscope equipped with a CCD camera, to record real-time videos of the system dynamics, and analyze different subsets of a total field of view of $145 \times 108\mu m^2$.
- [37] We note that if driven along a crystallographic axis, the particle transport is rather stable, and the dynamics shows a transition from a synchronous to asynchronous transport when ω is increased, as reported for a similar one-dimensional system [44], see also Fig.S2 in [32].
- [38] A. V. Straube and P. Tierno, *Soft Matter*, **10**, 3915 (2014).
- [39] M. Zborowski and J. J. Chalmers, *Magnetophoresis: Fundamentals and Applications* (Wiley, London, 1985) pp. 1–23.
- [40] J. Wiersig and K.-H. Ahn, *Phys. Rev. Lett.*, **87**, 026803 (2001).
- [41] A. Vanossi, N. Manini, M. Urbakh, S. Zapperi, and E. Tosatti, *Rev. Mod. Phys.*, **85**, 529 (2013).
- [42] W. F. Druyvesteyn, D. L. A. Tjaden, and J. W. F. Dorleijn, *Philips Res. Repts.*, **27**, 7 (1972).
- [43] A. Soba, P. Tierno, T. M. Fischer, and F. Saguès, *Phys. Rev. E*, **77**, 060401 (2008).
- [44] A. V. Straube and P. Tierno, *Europhys. Lett.*, **103**, 28001 (2013).